In Silico Pharmacology (2026) 14:134
https://doi.org/10.1007/s40203-026-00626-3

RESEARCH

Integrated in silico investigation of an androstendiol derivative (monoxetanol) as a potential anti-prostate cancer agent: insights from molecular docking, MD simulations, MM/PBSA, ADMET, and DFT analyses

Yahia Bekkar[1] · Lanez Elhafnaoui[1] · Najim A. Al-Masoudi[2,3] · Nabeel A. Abdul-Rida[4] · Wasfi A. Al-Masoudi[5] · Ali M. Mahdi[6]

Received: 1 February 2026 / Accepted: 2 April 2026

Abstract

A novel androstendiol derivative, monoxetanol (MON), was synthesized from androsta-5,15-diene-3β-ol-17-one via a multistep route and evaluated for its anticancer potential. In vitro cytotoxicity was assessed using an MTT assay against human prostate cancer cell lines PC-3 and LNCaP-AI. MON exhibited marked cytotoxicity, with inhibition rates of 79.8% (PC-3) and 64.7% (LNCaP-AI) at 10.0 µM. To rationalize these effects and explore its therapeutic potential, an integrated in silico approach comprising molecular docking, ADMET prediction, molecular dynamics (MD) simulations, MM/PBSA binding free energy calculations, and density functional theory (DFT) analyses was performed, using abiraterone (ABT) as a reference. Docking results indicated that MON displayed consistently stronger binding affinities toward key oncogenic targets, including epidermal growth factor receptor (EGFR), cytochrome P450 17A1 (CYP17A1), and extracellular signal-regulated kinase 2 (ERK2). ADMET profiling suggested favorable pharmacokinetic properties and drug-likeness, with no major toxicity concerns. MD simulations confirmed the conformational stability of MON–protein complexes, supported by favorable MM/PBSA binding free energies predominantly driven by van der Waals and electrostatic contributions. Per-residue decomposition highlighted a broader and more favorable interaction network for MON, particularly within CYP17A1 and ERK2 active sites. DFT calculations further revealed a larger HOMO–LUMO energy gap for MON than ABT in both gas and aqueous phases, indicating enhanced chemical stability. Collectively, these findings position MON as a promising lead scaffold for further optimization and experimental validation in prostate cancer therapy.

Keywords Monoxetanol (MON) · Cytotoxicity · Molecular docking · Molecular dynamics · DFT study · ADMET prediction

✉ Lanez Elhafnaoui
lanez-elhafnaoui@univ-eloued.dz

✉ Najim A. Al-Masoudi
Najim.al-masoudi@gmx.de

[1] Laboratory of Valorisation and Technology of Saharian Resources (VTRS), Department of Process Engineering and Petrochemistry, Faculty of Technology, University of El Oued, 39000 El Oued, Algeria

[2] Department of Chemistry, College of Science, University of Basrah, Basrah, Iraq

[3] Present address: Constance, Germany

[4] Department of Chemistry, College of Science, University of Qadisiyah, Diwanyiah, Iraq

[5] Department of Physiology and Chemistry, College of Veterinary, University of Basrah, Basrah, Iraq

[6] Najaf Education Directorate, Ministry of Education, Najaf City, Iraq

Published online: 07 May 2026

Introduction

Prostate cancer (PCa) is the second most common invasive malignancy among men worldwide (Kania et al. 2025). The enzyme 17α-hydroxylase/C17,20-lyase (CYP17A1), a cytochrome P450 monooxygenase, plays a pivotal role in androgen and corticosteroid biosynthesis and has emerged as a critical therapeutic target in prostate cancer therapy (Kmeťová Sivoňová et al. 2017). Pharmacological inhibition of CYP17A1 suppresses androgen production and represents a central strategy in both clinical treatment and drug development for advanced PCa (Hartmann et al. 2002; Vasaitis et al. 2011). Steroidal derivatives bearing five- or six-membered 17β-exo nitrogen-containing heterocycles, including steroidal azoles, have demonstrated potent inhibition of CYP17A1 (Njar et al. 1998). These compounds block early steps in adrenal androgen synthesis and therefore hold significant promise as anti-prostate cancer agents (Moreira et al. 2008a,b). In 2005, Handratta et al. 2005reported the synthesis of galeterone (Fig. 1, compound **1**) and its Δ^4-3-keto derivative as steroidal antiandrogens. Galeterone was later developed by Tokai Pharmaceuticals as a dual-action therapeutic agent targeting CYP17A1 for prostate cancer treatment (Vasaitis et al. 2008). However, patients with castration-resistant prostate cancer (CRPC) have shown significant benefit from the FDA-approved CYP17A1 inhibitor abiraterone acetate (Zytiga, compound **2**) (Potter et al. 1995, Bryce and Ryan 2012). In parallel, Hartmann and co-workers synthesized several novel CYP17 inhibitors, reinforcing the therapeutic relevance of CYP17A1 blockade in prostate carcinoma (Hu et al. 2010).

Building on our recent work on the synthesis and pharmaceutical activity of D-ring-modified steroids at the C-3 and C-17 positions (Abdul-Rida et al. 2021; Al-Masoudi et al. 2014; Al-Masoudi et al. 2018; Al-Masoudi et al. 2016; Al-Masoudi et al. 2015a; Al-Masoudi et al. 2015b; Banday et al. 2021), we report here an integrated in silico investigation of our newly synthesized steroid, monoxetanol. Molecular docking, MD simulations, MM/PBSA binding free energy calculations, ADME–tox profiling, and density functional theory (DFT) analyses were performed to support its potential activity against prostate cancer.

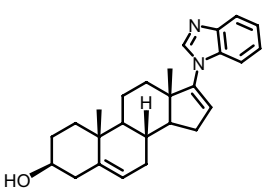

1. Galeterone

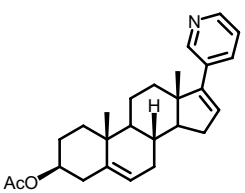

2. Abiratirone acetate

Fig. 1 Potent steroidal CYP17A1 inhibitors as therapeutic agents for prostate cancer

Results and discussion

Chemistry

((Androsta-5-ene-3β,17β-diol-15α-yl)thio)propanehydrazide (**6**) was previously synthesized in our laboratory (Abdul-Rida et al. 2021) from the readily available steroid androsta-5,15-diene-3β-ol-17-one (**3**) through a multistep synthetic route. Compound **6** was subsequently reacted with the non-steroidal anti-inflammatory drug naproxen in the presence of phosphoryl chloride ($POCl_3$) at 80–90 °C for 8 h. After chromatographic purification, this reaction afforded the target derivative, 15α-((2-(5-(1-(6-methoxynaphthalen-2-yl)ethyl)-1,3,4-oxadiazol-2-yl)ethyl)thio)-androsta-5-ene-3β,17β-diol (abbreviated as MON), in 52% isolated yield (Scheme 1).

The structure of MON was confirmed by ^{1}H and ^{13}C NMR spectroscopy. In the ^{1}H NMR spectrum, two multiplets at δ 2.91 and 2.75 ppm were assigned to the methylene protons of the $\underline{CH_2}CH_2S$ and $CH_2\underline{CH_2}S$ groups, respectively. A triplet at δ 5.32 ppm ($J_{6,7}$=2.2 Hz) corresponded to the olefinic H-6 proton. A broad singlet at δ 4.07 ppm was attributed to the 3-OH proton, overlapping with the methine proton of the $\underline{CH}$Me group, while a singlet at δ 3.88 ppm was assigned to the 17-OH proton. Multiplets at δ 2.35 and 2.19 ppm were ascribed to H-4a/H-7a and H-4b/H-7b/H-16b, respectively. Additional multiplets at δ 3.40, 3.25, and 2.52 ppm were assigned to H-17, H-3, and H-15, respectively. The remaining aliphatic protons resonated between δ 1.71 and 0.95 ppm. Aromatic proton signals were fully characterized in the Experimental section.

In the ^{13}C NMR spectrum, downfield resonances at δ 164.4 and 160.4 ppm were assigned to C-2 and C-5 of the oxadiazole ring. Signals at δ 31.7 and 29.5 ppm corresponded to the carbon atoms of the $\underline{CH_2}CH_2S$ and $CH_2\underline{CH_2}S$ groups. Resonances at δ 141.9, 75.4, 67.4, and 55.7 ppm were attributed to C-5, C-17, C-3, and C-9 of the androstenediol backbone, respectively. Additional signals at δ 48.9, 45.1, and 44.7 ppm were assigned to C-14, C-13, and C-4, together with the $\underline{CH}$Me carbon. The resonances at δ 37.1 and 36.1 ppm were attributed to C-1, C-10, and C-12, while the signal at δ 34.2 ppm corresponded to C-16. Furthermore, the resonances at δ 31.3 and 30.7 ppm were assigned to C-2, C-6, and C-7, and to C-8 and C-15, respectively. The resonance at δ 20.4 ppm was attributed to C-11 together with the methyl carbon of the CH$\underline{Me}$ group. Aromatic carbon signals were fully characterized in the Experimental section.

In vitro cytotoxic activity

The anticancer activity of the newly synthesized steroid MON was evaluated in vitro using the MTT assay (Mosmann 1983) against human prostate carcinoma cell lines (PC-3 and LNCaP-AI) and normal human prostatic epithelial cells

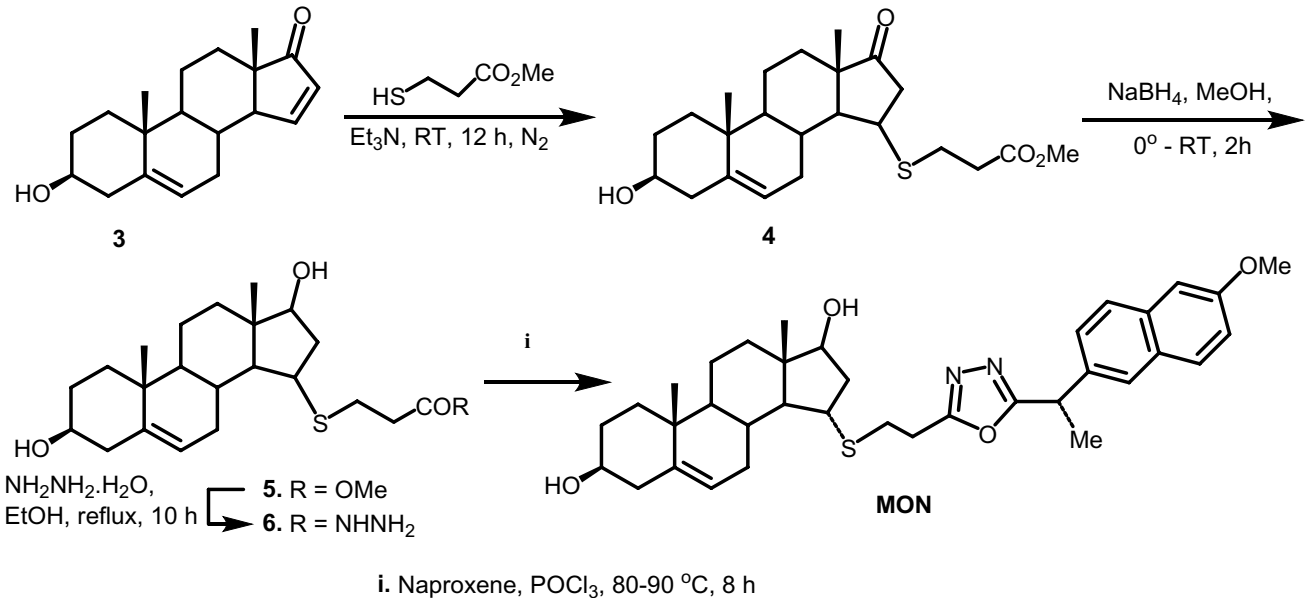

Scheme 1 Synthesis of steroid (monoxetanol) from androsta-5,15-diene-17-one analog **3**

Table 1 In vitro cytotoxic activity of MON and ABT after 72 h at 10 µM

Compd	Cytotoxic(%)		
	PC-3[a]	LNCaP-AI[a]	RWPE1[b]
MON	79.8	64.7	0.5%
ABT	92.4	nd	1.2%

[a]% inhibition from three independent experiments at 10 µM; [b]RWPE1: human prostatic epithelial cell lines

Table 2 RMSD values (Å) and predicted binding affinities (kcal/mol) of the native ligands, MON, and ABT against EGFR, CYP17A1, and ERK2

Target	EGFR	CYP17A1	ERK2
RMSD	1.783	0.398	0.678
NL	− 7.55	− 9.44	− 7.90
MON	− 10.64	− 13.67	− 11.51
ABT	− 9.78	− 10.13	− 9.41

(RWPE-1). ABT was employed as a positive control. The results are summarized in Table 1. After 72 h of treatment at 10 µM, MON exhibited significant cytotoxic activity against PC-3 and LNCaP-AI cells, with inhibition values of 79.8% and 64.7%, respectively, while displaying negligible toxicity toward RWPE-1 cells (0.5%). In comparison, ABT showed stronger growth inhibition against PC-3 cells (92.4%) but was also associated with measurable toxicity toward RWPE-1 cells (1.2%).

Computational studies

Molecular docking study

Binding affinity analysis The reliability of the molecular docking protocol was first validated by re-docking the co-crystallized native ligands into the active sites of EGFR (PDB ID: 1M17), CYP17A1 (PDB ID: 3RUK), and ERK2 (PDB ID: 4ZZN). Superimposition of the re-docked poses with their corresponding crystallographic conformations showed good agreement, yielding RMSD values of 1.783 Å for EGFR, 0.398 Å for CYP17A1, and 0.678 Å for ERK2 (Table 2). All RMSD values were below the accepted threshold of 2.0 Å, confirming that the docking protocol could reliably reproduce the experimental binding modes and validating the accuracy of the docking setup (Fig. 2).

The predicted binding affinities of the native ligands (NL), MON, and ABT toward the three-prostate cancer–related targets are summarized in Table 2. Overall, MON exhibited consistently stronger binding affinities than both the native ligands and the ABT across all investigated targets, indicating a favorable interaction profile. In the case of CYP17A1, a key enzyme in androgen biosynthesis, the NL displayed a binding energy of − 9.44 kcal/mol, whereas ABT showed an affinity of− 10.13 kcal/mol. MON exhibited the strongest interaction, with a binding energy of− 13.67 kcal/mol, indicating a substantially higher predicted affinity toward this validated therapeutic target. While CYP17A1 targeting is associated with inhibition of androgen biosynthesis, EGFR and ERK2 represent complementary non-androgen

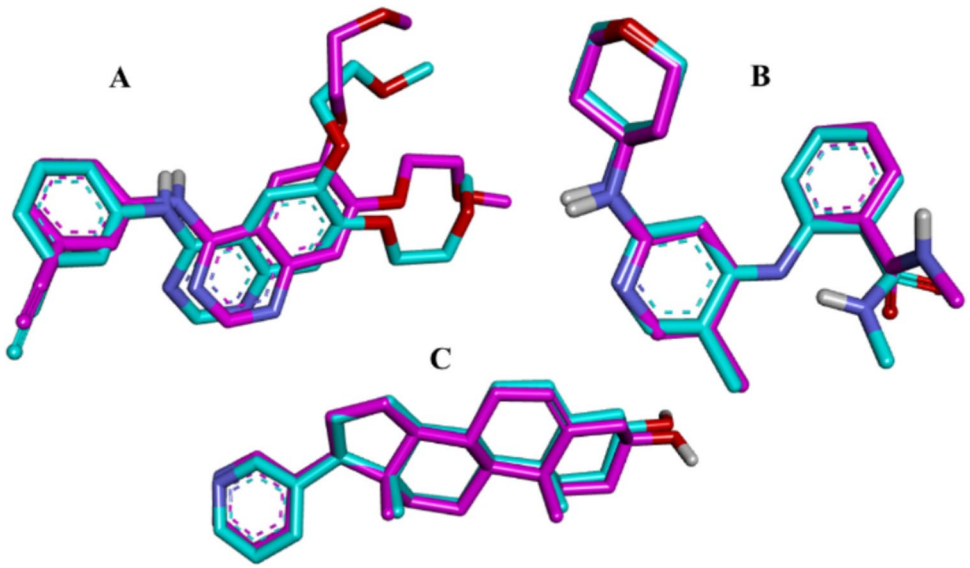

Fig. 2 Superimposition of co-crystallized native ligands (magenta) and re-docked poses (green) within the active sites **A** EGFR, **B** ERK2, and **C** CYP17A1

signaling pathways involved in tumor progression and resistance, supporting their inclusion in this study.

EGFR is a well-established target in prostate cancer, particularly in the transition to castration-resistant prostate cancer (CRPC), where it can act as an alternative pathway bypassing androgen receptor (AR) signaling (Schlomm et al. 2017). In this study, the NL showed a binding energy of − 7.55 kcal/mol, while ABT bound with an affinity of − 9.78 kcal/mol. Notably, MON demonstrated a stronger interaction with EGFR, exhibiting a binding energy of − 10.64 kcal/mol, suggesting enhanced stabilization within the EGFR active site.

ERK2 (Extracellular Signal-Regulated Kinase 2), a key component of the MAPK/ERK signaling pathway, plays a critical role in prostate cancer progression by regulating cell proliferation, survival, and metastasis (Chen et al. 2013, 2017). For ERK2, the NL bound with an affinity of − 7.90 kcal/mol, while ABT exhibited a binding energy of − 9.41 kcal/mol. MON again showed superior binding, with a binding energy of − 11.51 kcal/mol, suggesting strong stabilization within the ERK2 binding pocket.

Collectively, the docking results demonstrate that MON consistently outperforms ABT and the native ligands in terms of predicted binding affinity across all examined targets. The particularly strong interaction observed with CYP17A1 is noteworthy given its central role in prostate cancer therapy. These findings suggest that MON possesses a favorable molecular interaction profile and justify its further evaluation using molecular dynamics simulations and MM/PBSA binding free energy calculations.

Interaction analysis with BSA For EGFR, the NL formed hydrogen bonds with MET98 and GLY101 (2.65–3.98 Å) and hydrophobic contacts with VAL31, LYS50, LEU93, THR95, and LEU149 (2.74–3.96 Å) (Table S1). ABT interacted through a hydrogen bond with THR95 (3.38 Å), hydrophobic contacts with ALA48, LYS50, LEU82, LEU93, THR95, and MET98, and a salt bridge with LYS50 (5.00 Å). In contrast, MON exhibited enhanced stabilization, forming hydrogen bonds with LYS50 and GLU67 (2.65–3.96 Å) and extensive hydrophobic interactions with LEU23, VAL31, ALA48, LYS50, LEU97, MET98, LEU149, and THR159 (3.09–3.77 Å), indicating improved complementarity within the EGFR active site (Fig. 3).

In the CYP17A1 binding site, the NL formed a hydrogen bond with ASN172 (2.03 Å) and hydrophobic interactions with ALA83, PHE84, ILE175, ALA263, and VAL443 (3.38–3.97 Å) (Table S2). ABT engaged in hydrogen bonds with ARG209, ILE404, and GLY405 (2.95–4.09 Å) and hydrophobic contacts with ALA83, ILE175, ILE176, ALA263, GLU266, THR267, and ILE332 (3.39–3.86 Å). Notably, MON formed multiple hydrogen bonds with ARG209, ALA263, and ALA409 (3.04–3.61 Å), together with extensive hydrophobic interactions involving ALA83, PHE84, ILE176, ASP259, ILE260, ALA263, GLU266, ILE332, ILE404, LEU408, VAL443, and VAL444 (3.09–3.83 Å), reflecting stronger stabilization within the CYP17A1 binding pocket (Fig. 4).

For ERK2, the NL formed a hydrogen bond with MET98 (2.87–2.98 Å) and hydrophobic contacts with ILE21, VAL29, ALA42, and GLN95 (3.41–3.99 Å) (Table S3). ABT established hydrogen bonds with ARG57, MET98, ASN144, and ASP156 (2.86–3.76 Å), hydrophobic interactions with ALA25, VAL29, LYS44, and LEU146 (3.31–3.58 Å), and a salt bridge with LYS141 (3.45 Å). MON exhibited multiple hydrogen bonds with GLU23, LYS44, GLU99, LYS141, SER143, and ASP156 (2.54–4.00 Å), and

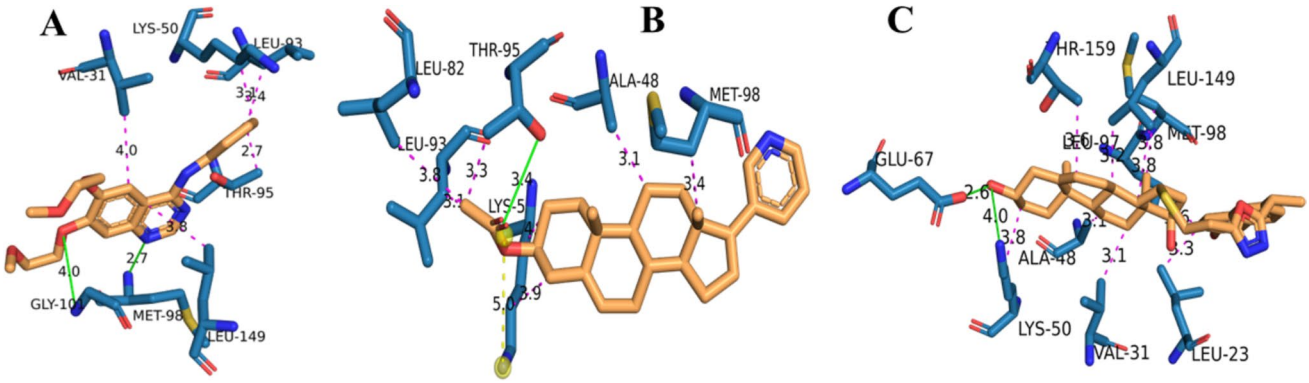

Fig. 3 3D binding interactions of **A** NL, **B** ABT, and **C** MON within the EGFR active site

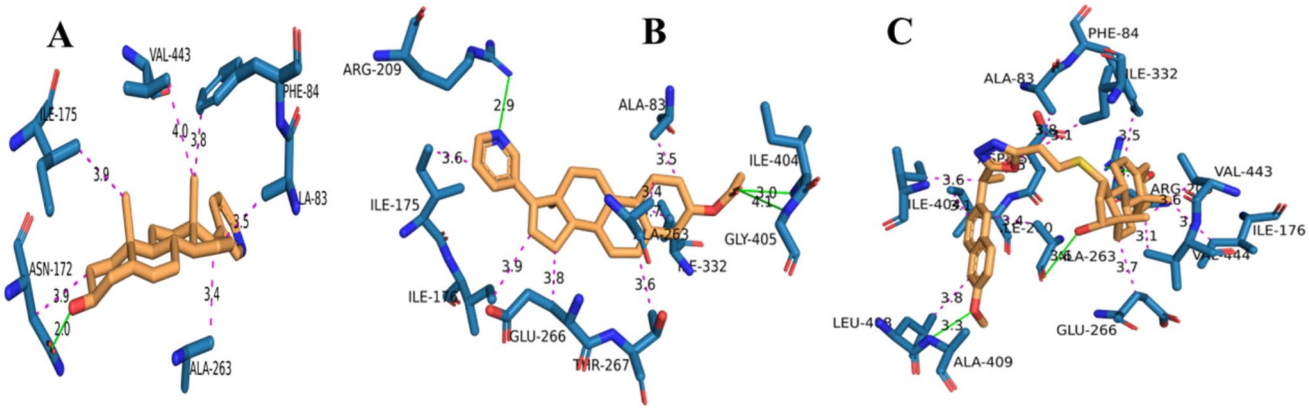

Fig. 4 3D binding interactions of **A** NL, **B** ABT, and **C** MON within the CYP17A1 active site

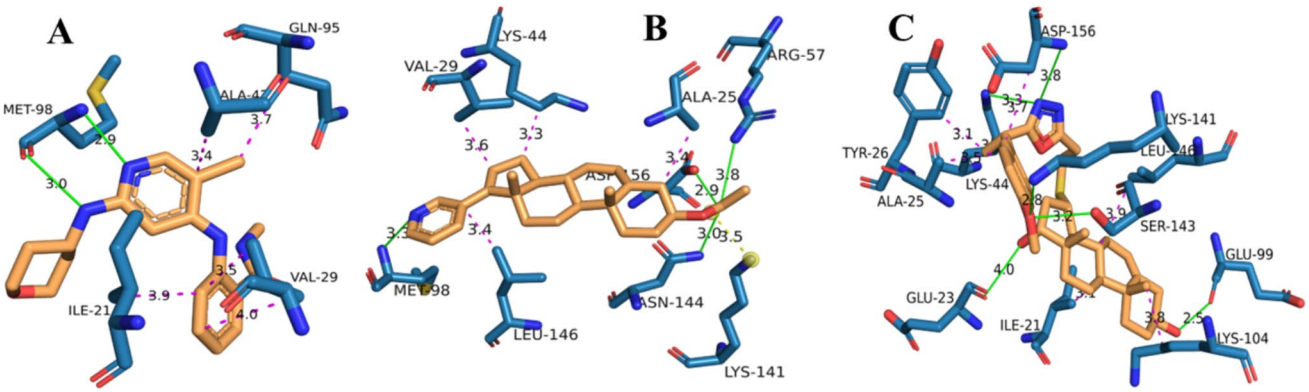

Fig. 5 3D binding interactions of **A** NL, **B** ABT, and **C** MON within the ERK2 active site

hydrophobic interactions involving ILE21, ALA25, TYR26, LYS44, LYS104, and LEU146 (3.12–3.93 Å), indicating a more extensive and cohesive interaction network within the ERK2 active site (Fig. 5).

Overall, MON consistently exhibited more hydrogen bonds and hydrophobic contacts across all three targets compared with ABT and the native ligands. This expanded interaction network provides a structural rationale for its more favorable docking scores and supports its predicted higher binding stability.

ADMET and drug-likeness evaluation

The pharmacokinetic and toxicity profiles of ABT acetate and MON were assessed using in silico ADMET predictions (Table 3) to evaluate their drug-likeness, bioavailability, and safety characteristics. ABT exhibited high gastrointestinal (GI) absorption, consistent with its moderate molecular weight (399.61 g/mol), low topological polar surface area (TPSA = 38.33 $Å^2$), and favorable lipophilicity (consensus LogP = 4.92). In contrast, MON showed low predicted GI

Table 3 In silico ADME properties, drug-likeness parameters, and toxicity predictions of ABT. and MON

Parameter	ABT	MON	Parameter	ABT	MON
MW (g/mol)	399.61	602.83	CYP3A4	No	No
Num HBA	3	6	Log Kp (cm/s)	− 4.70	− 4.97
Num HBD	1	2	Lipinski	Yes 1V	No 2V
Consensus LogP	4.92	6.24	Ghose	Yes	No 4V
TPSA (Å^2)	38.33	113.91	Veber	Yes	Yes
LogS (ESOL)	− 5.70	− 7.82	Egan	Yes	No 1V
GI absorption	High	Low	Muegge	No 1V	No 1V
P-gp substrate	No	No	BAS	0.55	0.17
BBB permeant	Yes	No	Carcinogenicity	Inact70%	Inact51%
LD_{50} (mg/kg)	830	560	Immunotoxicity	Act87%	Act99%
Toxicity class	4	4	Mutagenicity	Inact85%	Inact63%
Hepatotoxicity	Inact61%	Inact52%	Cytotoxicity	Inact83%	Inact74%

MW: molecular weight; HBA: hydrogen bond acceptors; HBD: hydrogen bond donors; TPSA: total polar surface area; GI gastrointestinal: P-gp: P glycoprotein; BAS: bioavailability scores; V: violation; Act: Active; Inact: Inactive

Table 4 MD simulation parameters of ABT and MON complexes with EGFR, CYP17A1, and ERK2

	EGFR		CYP17A1		ERK2	
	ABT	MON	ABT	MON	ABT	MON
RMSD (nm)	0.739	0.818	0.283	0.341	0.155	0.225
RMSF (nm)	0.275	0.387	0.113	0.108	0.083	0.094
SASA (nm^2)	190.405	187.772	221.157	220.573	162.591	160.143
Rg (nm)	2.363	2.349	2.308	2.311	2.139	2.182
H-bond	0.089	1.010	0.204	1.767	0.139	0.818

absorption, attributable to its high molecular weight (602.83 g/mol) and elevated polarity (TPSA = 113.91 Å^2), which are known to limit passive intestinal permeability.

Both compounds were predicted not to be P-glycoprotein (P-gp) substrates, suggesting a reduced risk of efflux-mediated bioavailability loss. Skin permeability values (log Kp) indicated low dermal penetration for both ligands, with slightly lower permeability predicted for MON. ABT was predicted to be blood–brain barrier (BBB) permeant, in line with its high lipophilicity and low TPSA, whereas MON was not BBB permeant, likely due to its larger size and increased polarity. Neither compound was predicted to inhibit CYP3A4, suggesting a low potential for drug–drug interactions.

Regarding drug-likeness, ABT satisfied most rule-based filters, with only one Lipinski violation related to lipophilicity (MLOGP > 4.15). It complied with the Ghose, Veber, Egan, and Muegge criteria, reflecting an overall acceptable medicinal chemistry profile. In contrast, MON violated multiple rules across Lipinski, Ghose, Egan, and Muegge filters, primarily due to excessive molecular weight and high lipophilicity, which are expected to compromise oral bioavailability despite compliance with Veber's rule. Its predicted bioavailability score (0.17) was markedly lower than ABT (0.55), indicating a need for caution in oral administration.

Toxicity predictions classified both compounds into toxicity class 4, indicative of moderate acute toxicity, with MON showing slightly lower predicted LD_{50} (560 mg/kg vs. 830 mg/kg for ABT). Neither compound was predicted to be carcinogenic, mutagenic, hepatotoxic, or cytotoxic, with high inactivity probabilities. However, immunotoxicity was predicted as active for both ligands, with a notably higher probability for MON (99%) than for ABT (87%).

Collectively, ABT demonstrated a more favorable ADMET profile, with superior absorption, bioavailability, and overall drug-likeness (Pires et al. 2015). Although MON exhibited promising docking and interaction profiles, its suboptimal absorption properties and multiple drug-likeness violations highlight potential limitations for oral bioavailability and systemic exposure. To address these challenges, structural optimization, such as reducing molecular size or polarity, or formulation strategies, including nanoparticle-based delivery or prodrug design, could be pursued to improve absorption and drug-likeness while retaining anticancer activity.

MD simulation analysis

Molecular dynamics (MD) simulations were conducted to evaluate the structural stability, flexibility, compactness, and intermolecular interactions of the ABT– and MON–protein complexes with EGFR, CYP17A1, and ERK2. The dynamic behavior of the complexes was analyzed using RMSD, RMSF, radius of gyration (Rg), SASA, and hydrogen bond (H-bond) metrics, as summarized in Table 4 and Fig. 6.

The RMSD profiles (Fig. 6A) showed that most complexes reached equilibrium within the first 3 ns and remained stable throughout the simulation. An exception was observed for the EGFR–MON system, which exhibited a

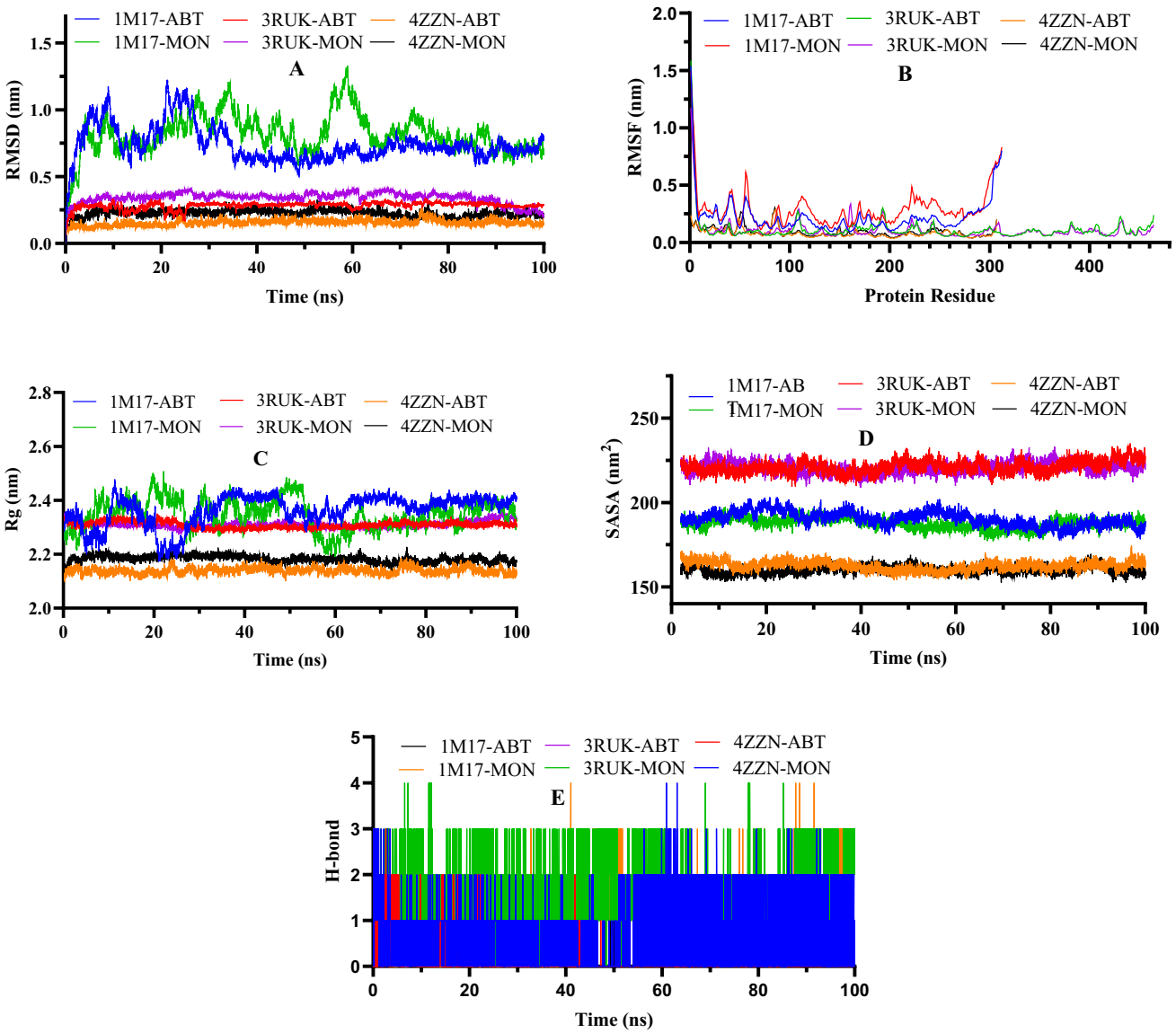

Fig. 6 Molecular dynamics analysis of ABT and MON complexes: **A** RMSD, **B** RMSF, **C** Rg, **D** SASA, and **E** number of H-bonds

prolonged equilibration phase, stabilizing at approximately 65 ns compared to ~ 35 ns for ABT. This behavior suggests progressive conformational adaptation of EGFR to MON. After equilibration, both EGFR complexes remained stable with comparable RMSD values, confirming the formation of persistent binding conformations. In the CYP17A1 and ERK2 systems, ABT displayed marginally lower average RMSD values; however, the RMSD values observed for MON (0.341 nm for CYP17A1 and 0.225 nm for ERK2) remained well within the accepted range for stable protein–ligand complexes, indicating robust structural stability.

The comparatively higher RMSD values observed for the EGFR complexes likely reflect intrinsic domain flexibility in EGFR and ligand-induced conformational rearrangements rather than complex instability, as supported by the stable Rg and SASA profiles. The RMSF analysis (Fig. 6B) revealed that MON induced slightly higher residue-level fluctuations in EGFR (0.387 nm) compared to ABT (0.275 nm). For CYP17A1 and ERK2, RMSF values for MON were comparable to those of ABT, indicating that MON binding does not induce unfavorable global flexibility and preserves the structural integrity of the proteins.

The radius of gyration profiles (Fig. 6C) demonstrated that all complexes maintained an overall compact structure throughout the simulation. In EGFR, MON exhibited early-stage Rg fluctuations, consistent with its longer equilibration phase observed in the RMSD analysis. Following equilibration, the EGFR–MON complex stabilized with an average Rg value (2.349 nm) comparable to that of ABT (2.363 nm), indicating equivalent final compactness. For CYP17A1,

both ABT and MON complexes showed nearly identical Rg values (~2.31 nm), while in ERK2, the ABT complex exhibited a slightly lower average Rg (2.139 nm) than MON (2.182 nm), suggesting marginally enhanced compactness. Overall, these results confirm that MON preserves protein compactness across all targets.

The SASA profiles (Fig. 6D) showed comparable solvent exposure for ABT- and MON-bound complexes across all proteins. Notably, MON exhibited slightly lower SASA values for EGFR and ERK2 compared to ABT, suggesting improved burial of the ligand within the binding pocket, a feature commonly associated with enhanced binding stability. Hydrogen bond analysis (Fig. 6E) revealed that MON formed a higher average number of hydrogen bonds with all three protein targets compared to ABT. In particular, MON exhibited substantially stronger hydrogen bonding with CYP17A1 (1.767 vs. 0.204) and ERK2 (0.818 vs. 0.139), indicating more persistent polar interactions that likely contribute to its stable binding mode.

Although ABT demonstrated marginally lower RMSD values in certain systems, MON consistently exhibited stronger intermolecular interactions, enhanced hydrogen bonding, and comparable compactness across all targets. The adaptive conformational changes observed upon MON binding, particularly in EGFR, suggest a stable and well-accommodated binding mode.

Collectively, these findings support MON as a dynamically stable ligand and a promising alternative to the reference drug ABT, despite its less favorable ADMET profile.

MM/PBSA binding free energy analysis

The MM/PBSA method was applied to quantify the binding energetics of MON and ABT toward EGFR, CYP17A1, and ERK2. The decomposed energetic components and total binding free energies are summarized in Table S4 and illustrated in Fig. 7.

Across all three targets, MON exhibited significantly more favorable total binding free energies (ΔG_{bind}) than ABT, indicating stronger and more stable complex formation. In the EGFR system, MON achieved a ΔG_{bind} of − 72.26 ± 7.04 kcal/mol, compared to − 58.31 ± 4.80 kcal/mol for ABT. This enhancement is primarily attributable to substantially stronger van der Waals (ΔE_{vdW}) and electrostatic (ΔE_{ele}) contributions, reflecting improved shape complementarity and reinforced polar interactions within the binding pocket. A similar trend was observed for CYP17A1, where MON displayed the most favorable binding among all studied systems, with a ΔG_{bind} of − 106.48 ± 5.40 kcal/mol, significantly exceeding that of ABT (− 67.52 ± 5.24 kcal/mol). The dominant contribution arose from highly favorable gas-phase interaction energies (ΔG_{Gas}), particularly van der Waals interactions (− 80.78 ± 2.86 kcal/mol), highlighting strong hydrophobic packing and close ligand–protein contacts. These findings are consistent with the compact binding mode and elevated hydrogen bond persistence observed during the MD simulations.

In the ERK2 complexes, MON again outperformed ABT, exhibiting a ΔG_{bind} of − 55.54 ± 5.99 kcal/mol versus − 32.63 ± 5.85 kcal/mol for ABT. Notably, MON formed significantly stronger electrostatic interactions with ERK2, consistent with the higher number and stability of hydrogen bonds identified in the MD trajectories, underscoring the role of polar interactions in stabilizing this complex. Although MON incurred higher polar solvation penalties (ΔE_{PB}) than ABT across all systems, these unfavorable contributions were fully compensated by markedly stronger van der Waals, electrostatic, and nonpolar solvation (ΔE_{NPB}) terms. This energetic balance suggests deep insertion of MON into the binding cavities, enabling extensive hydrophobic and electrostatic contacts despite increased desolvation costs.

Collectively, the MM/PBSA results strongly corroborate the molecular docking and MD simulation findings, confirming that MON consistently exhibits superior binding affinity and interaction strength relative to ABT across all investigated targets. While the absolute free energies may be affected by the omission of entropic contributions, the relative trends strongly support MON as a promising

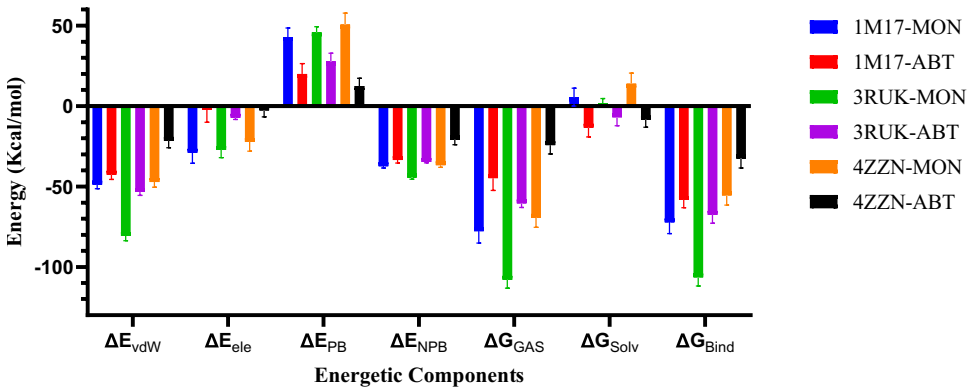

Fig. 7 Decomposition of MM/PBSA binding free energy components for MON and ABT complexes with EGFR (1M17), CYP17A1 (3RUK), and ERK2 (4ZZN)

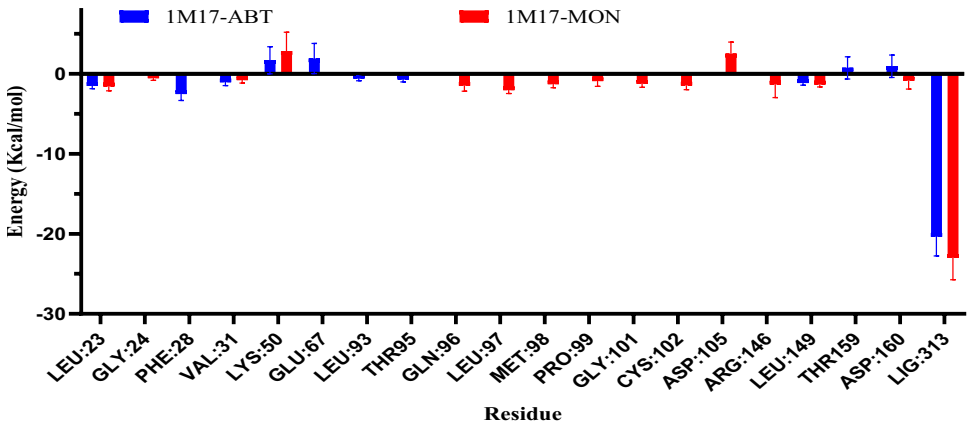

Fig. 8 Per-residue binding free energy decomposition for ABT and MON complexes with EGFR (1M17)

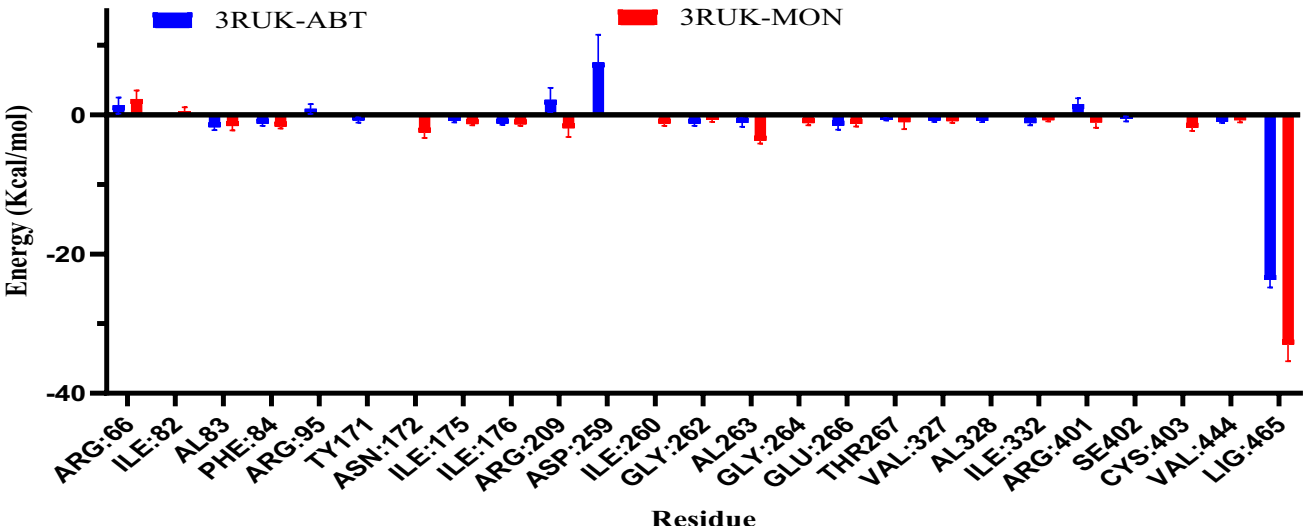

Fig. 9 Per-residue binding free energy decomposition for ABT and MON complexes with CYP17A1 (3RUK)

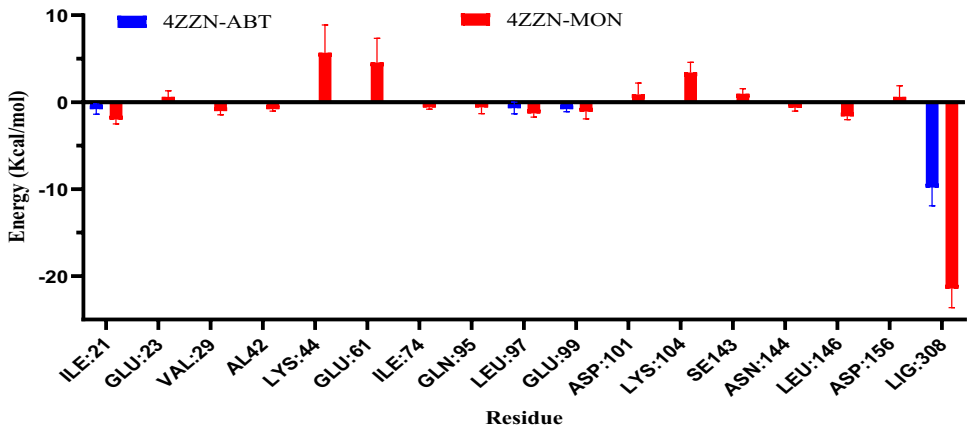

Fig. 10 Per-residue binding free energy decomposition for ABT and MON complexes with ERK2 (4ZZN)

lead compound for subsequent structural optimization and experimental validation.

Per-residue binding free energy analysis

To identify key amino acid residues responsible for ligand stabilization and to rationalize the observed binding free energies, per-residue MM/PBSA energy decomposition was performed for the EGFR, CYP17A1, and ERK2 complexes. The residue-wise energy contributions are summarized in Tables S5–S7 and illustrated in Figs. 8, 9 and 10, respectively.

As shown in Fig. 8 and Table S5, both ligands interacted with residues lining the EGFR binding pocket; however,

MON exhibited a broader and more favorable interaction profile. MON formed stabilizing interactions with several key residues, including GLN96, LEU97, MET98, GLY101, and CYS102, which displayed moderate to strong negative energy contributions. In contrast, these residues contributed weakly or were not significantly involved in ABT binding. Notably, MON showed stronger ligand self-contributions (LIG: − 22.97 ± 2.77 kcal/mol) than ABT (− 20.34 ± 2.43 kcal/mol), indicating a more energetically favorable binding mode. Although both ligands exhibited unfavorable contributions from charged residues such as LYS50 and ASP105, the enhanced hydrophobic and polar contacts formed by MON compensated for these penalties, consistent with its improved total MM/PBSA binding free energy.

The per-residue decomposition for CYP17A1 (Fig. 9, Table S6) revealed pronounced differences between MON and ABT. MON established strong stabilizing interactions with multiple residues within the catalytic cavity, including ASN172 (− 2.51 ± 0.82 kcal/mol), ILE175, ILE176, ALA263 (− 3.68 ± 0.43 kcal/mol), CYS403, and GLY264. These residues contributed only weakly or not at all to ABT binding. Importantly, ABT exhibited a highly unfavorable contribution from ASP259 (7.48 ± 4.03 kcal/mol), which was absent in the MON complex, indicating reduced electrostatic strain upon MON binding. The ligand contribution term further confirmed the superiority of MON (LIG: − 32.95 ± 2.44 kcal/mol) compared to ABT (− 23.68 ± 1.13 kcal/mol), explaining the markedly stronger binding affinity of MON toward CYP17A1 observed in the total MM/PBSA analysis.

In the ERK2 system (Fig. 10, Table S7), MON again exhibited enhanced residue-level stabilization relative to ABT. MON formed favorable interactions with several hydrophobic and polar residues, including ILE21 (− 1.98 ± 0.53 kcal/mol), VAL29, LEU97, GLU99, ASN144, and LEU146, whereas ABT interacted with a more limited number of residues and with weaker energetic contributions. Although MON showed unfavorable contributions from charged residues such as LYS44 and GLU61, these effects were outweighed by strong ligand-centered stabilization (LIG: − 21.43 ± 2.19 kcal/mol), which was more than double that of ABT (− 9.81 ± 2.12 kcal/mol). This residue-level behavior corroborates the stronger total binding free energy and enhanced interaction persistence observed during the MD simulations.

Across all three protein targets, per-residue energy decomposition consistently demonstrated that MON engages a larger number of stabilizing residues and exhibits stronger ligand-centered energetic contributions than the reference drug ABT. The enhanced binding of MON is primarily driven by improved hydrophobic packing and favorable polar interactions, which compensate for occasional electrostatic penalties. These findings provide residue-level mechanistic support for the superior binding affinities of MON observed in docking, MD simulations, and MM/PBSA analyses.

DFT analysis

Frontier molecular orbital (FMO) theory provides insight into the electronic structure and reactivity of molecular systems through analysis of the highest occupied molecular orbital (HOMO) and lowest unoccupied molecular orbital (LUMO) (Bendaas et al. 2024). The HOMO–LUMO energy gap ($\Delta E = E_{LUMO} - E_{HOMO}$) reflects kinetic stability, chemical reactivity, and the potential for intramolecular charge transfer, which can influence ligand–protein interactions. The HOMO–LUMO distributions and corresponding molecular electrostatic potential (MEP) surfaces of MON and ABT in both gas and aqueous phases are shown in Figs. 11 and 12, while the calculated quantum chemical descriptors are summarized in Table 5.

For ABT, the HOMO and LUMO are mainly distributed over the 3-(cyclopentenyl)pyridine moiety, indicating that this region as the main site for electron donation and acceptance. In contrast, the HOMO and LUMO of MON are predominantly localized on the methoxynaphthalene scaffold and adjacent functional groups, suggesting these regions as the key pharmacophoric sites likely to participate in hydrogen bonding, π–π stacking, and electrostatic interactions within protein binding pockets. These patterns persist in both gas and aqueous phases, indicating intrinsic orbital stability under physiological-like conditions.

The MEP surfaces reveal distinct electrostatic features for MON and ABT (Figs. 11 and 12). In MON, electronegative regions are concentrated around the oxygen atoms of the hydroxyl and methoxy groups, as well as the nitrogen and oxygen atoms of the oxadiazole ring, identifying these sites as favorable hydrogen bond acceptors. while the electropositive region is primarily associated with the hydroxyl proton, indicates hydrogen bond donation capability. In contrast, ABT exhibits negative electrostatic regions mainly localized on the pyridine nitrogen and acetate oxygen, indicating fewer but more spatially confined interaction hotspots.

MON exhibits significantly lower HOMO energies than ABT in both environments (gas: − 7.79 vs. − 6.11 eV; water: − 7.85 vs − 6.11 eV), indicating reduced electron-donating ability. Conversely, ABT, with its higher HOMO energy, may act as a stronger electron donor. MON also displays higher LUMO energies than ABT, implying a lower electron-accepting tendency. Consequently, the HOMO–LUMO energy gap of MON is substantially larger than that of ABT in both phases (gas: 10.32 vs. 5.15 eV; water: 10.19 vs. 5.09

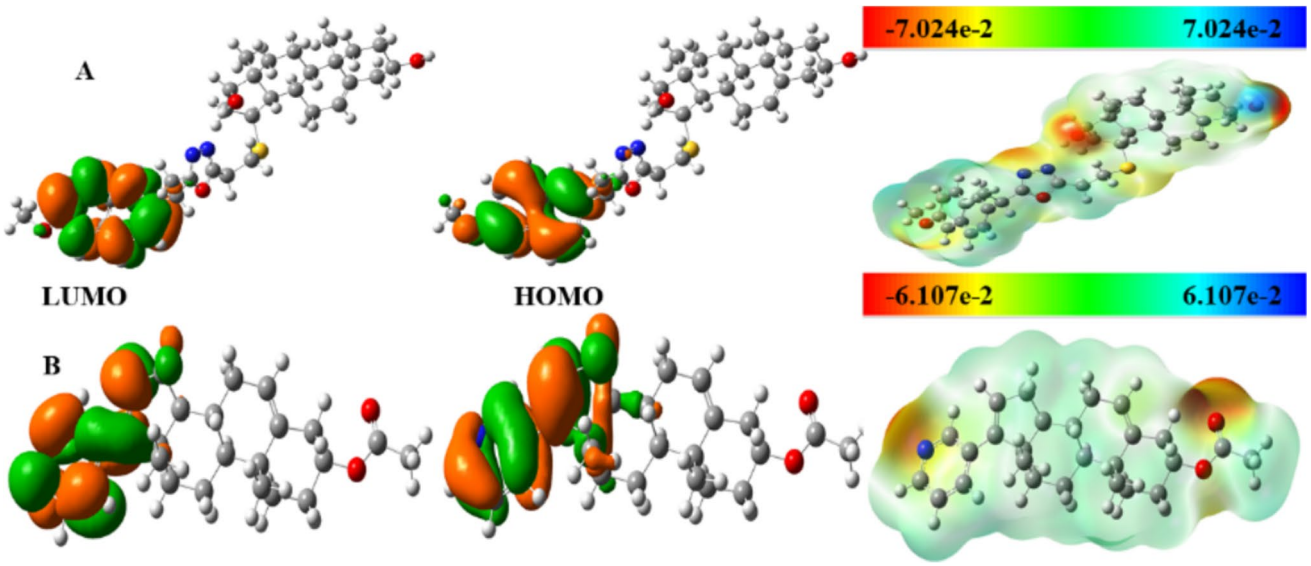

Fig. 11 HOMO, LUMO, and molecular electrostatic potential surfaces of **A** MON and **B** ABT in the gas phase

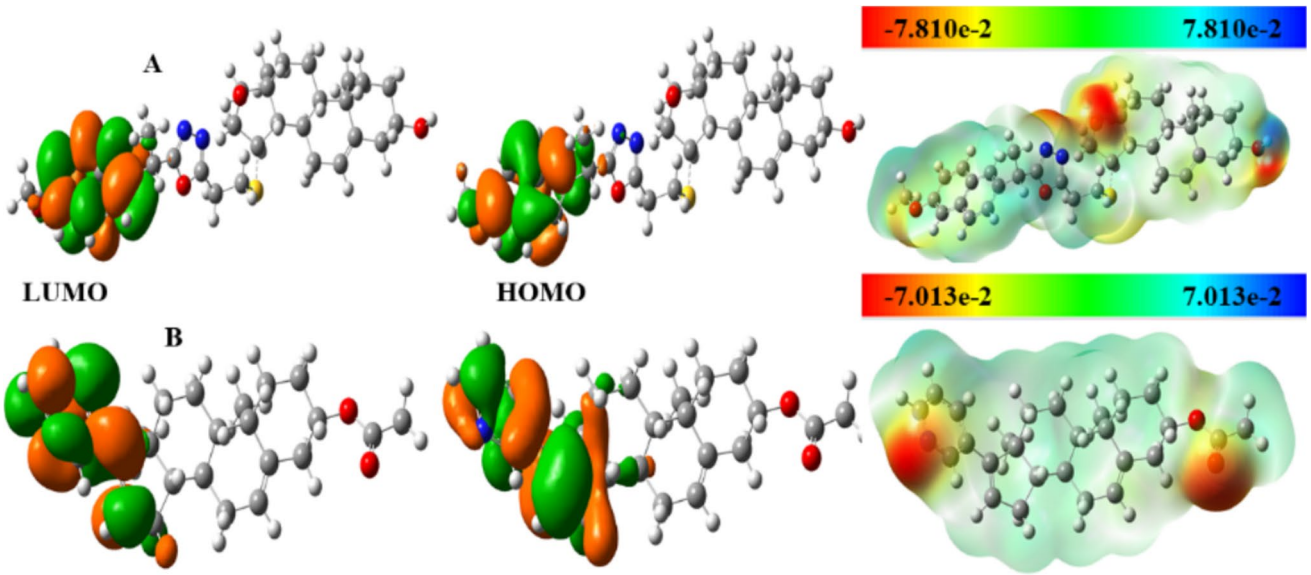

Fig. 12 HOMO, LUMO, and molecular electrostatic potential surfaces of **A** MON and **B** ABT in the aqueous phase

eV). A larger ΔE is generally associated with higher kinetic stability and lower chemical reactivity, whereas a smaller ΔE reflects increased softness and reactivity (Bendaas et al. 2024). Thus, ABT is predicted to be intrinsically more reactive, while MON demonstrates greater electronic stability, a favorable feature for minimizing nonspecific interactions in drug candidates.

The global reactivity descriptors derived from FMO energies (Table 5) further support these trends. MON displays higher global hardness (η) and lower softness (S) than ABT, confirming its resistance to electronic deformation. In addition, the electrophilicity index (ω) of MON is markedly lower than that of ABT in both phases, indicating that MON behaves as a weaker electrophile. This reduced electrophilic character may contribute to improved selectivity and a lower likelihood of off-target reactivity. Conversely, ABT shows higher electronegativity (χ) and electrophilicity, consistent with its smaller ΔE and greater chemical reactivity, which may enhance interaction strength but also increase susceptibility to nonspecific or metabolic reactions.

Collectively, the DFT results reveal that MON's stable electronic structure, well-defined frontier orbital localization, and complementary electrostatic profile facilitate favorable and selective interactions with EGFR, CYP17A1, and ERK2, providing a molecular rationale for its superior

Table 5 Frontier molecular orbital energies (eV) and global reactivity descriptors (eV) of MON and ABT calculated in the gas and aqueous phases

	Gas		Water	
	MON	ABT	MON	ABT
HOMO	− 7.79	− 6.11	− 7.85	− 6.11
LUMO	2.52	− 0.96	2.34	− 1.03
ΔE	10.32	5.15	10.19	5.09
IPE	7.79	6.11	7.85	6.11
EA	− 2.52	0.96	− 2.34	1.03
χ	2.63	3.54	2.75	3.57
μ	− 2.63	− 3.54	− 2.75	-3.57
η	5.16	2.58	5.10	2.54
S	0.10	0.19	0.10	0.20
ω	0.67	2.43	0.74	2.51
ω^-	2.64	4.52	2.76	4.61
ω^+	0.00	0.98	0.00	1.04

binding and reinforcing its potential as a robust lead compound for prostate cancer therapy.

Experimental

Materials and methods

Melting points were determined using a Büchi B-545 melting point apparatus (Büchi Labortechnik AG, Switzerland) and are reported uncorrected. NMR spectra were recorded on 400 MHz (^{1}H) and on 75 MHz (^{13}C) spectrometers (Bruker DPX-400, Germany) with tetramethylsilane (TMS) as an internal standard. Chemical shifts (δ) are reported in parts per million (ppm). Proton signal assignments were performed using selective proton decoupling or by COSY spectroscopy. Infrared (IR) spectra were recorded on a Shimadzu spectrophotometer. Thin-layer chromatography (TLC) was performed on silica gel 60 F254 plates (Merck), and chromatograms were visualized under UV light (254–266 nm) and by iodine vapor staining.

((Androsta-5-ene-3β,17β-diol-15α-yl)thio) propanehydrazide (6) (Abdul-Rida et al. 2021)

A mixture of methyl ((androsta-5-ene-3β,17β-diol-15α-yl) thio)propanoate (**4**) (500 mg, 1.23 mmol) and an excess of hydrazine hydrate (80%, 5 mL) in EtOH (15 mL) was heated under reflux for 10 h. Reaction progress was monitored by TLC using *n*-hexane–ethyl acetate (4:1) as the eluent. After completion, the reaction mixture was concentrated by evaporation and allowed to cool to room temperature. The resulting solid was filtered, dried, and recrystallized from ethanol to afford compound **6** (350 mg, 70% yield) as a yellow powder; m.p.: 152–153 °C; R_f=0.32; FTIR (ν_{max}, cm^{-1}): 3442 (OH), 3421, 3284 (NH_2), 2964, 2933 ($CH_{aliph.}$) 1660 ($C{=}O_{amide}$), 1633 (NH), 1633 (C=C). ^{1}H NMR (DMSO-d_6): δ 9.06 (s, 1H, NH_{amide}), 6.88 (br s., 2H, NH_2), 5.28 (t, 1H, $J_{6,7}$=2.3 Hz, H-6), 4.53 (br s., 1H, 3-OH), 3.72 (br s., 1H, 7-OH), 3.44 (m, 1H, H-17), 3.27 (br s., 1H, H-3), 3.06 (m, 1H, H-15), 2.64 (m, 2H, 2.67 (m, 2H, CH2- 21), 2.45 (m, 2H, CH2-22), 2.36 (m, 1H, H-16a), 2.31 (m, 1H, H-7a), 2.14 (m, 2H, CH_2-4), 1.81 (m, 1H, H-1a), 1.76 (m, 1H, H-12a), 1.68 (m, 1H, H-2a), 1.55 (m, 2H, H-8+H-16b), 1.55 (m, 1H, H-7b), 1.49 (m, 1H, H-11a), 1.39 (m, 1H, H-2b), 1.35 (m, 1H, H-11b), 1.25 (m, 1H, H-14), 0.96 (m, 4H, Me-19+H-12b), 0.83 (m, 2H, H-1b+H-9), 0.71 (s, 3H, Me-18). ^{13}C NMR (DMSO-d_6): δ 170.5 ($C{=}O_{amide}$), 141.6 (C-5), 120.9 (C-6), 80.5 (C-17), 70.5 (C-3), 54.4 (C-14), 50.5 (C-9), 43.6 (C-13+C-16), 42.7 (C-4+C-15), 37.7 (C-12) 37.5 (C-1), 36.7 (C-10+CH_2-22), 31.8 (C-2), 31.3 (C-7), 29.8 (C-8), 28.7 (CH_2-21), 20.5 (C-11), 19.5 (Me-19), 14.2 (Me-18). Anal. calc. for $C_{22}H_{36}N_2O_2S$ (408.60): C, 64.67; H, 8.88; N, 6.86. Found: C, 64.59; H, 8.80; N, 6.93.

15a-((2-(5-(1-(6-Methoxynaphthalen-2-yl)ethyl)-1,3,4-oxadiazol-2-yl)ethyl) thio)androsta-5-ene-3β,17β-diol (monoxetanol)

To a mixture of naproxene (75 mg, 0.32 mmol) in $POCl_3$ (8 mL) was added the steroid **6** (130 mg, 0.31 mmol) very slowly at room temperature. The mixture was heated at 80–90 °C for 8 h and the reaction was monitored by TLC (hexane–ethyl acetate 3:2). The reaction mixture was cooled and poured on ice-water to give a white product, which was partitioned between ethyl acetate (2 × 20 mL) and $NaHCO_3$ (20 mL) and the combined organic extract was dried (Na_2SO_4), filtered and evaporated to dryness. The residue was purified on a short column of silica gel (5 g), using hexane–ethyl acetate 3:2 as an eluent to give pure product **7** (mg, 52%) as a crystalline product, m.p. 158–161 °C, R_f=0.25; FTIR (ν_{max}, cm^{-1}): 3442 (OH), 2964, 2933 ($CH_{aliph.}$) 1660 ($C{=}O_{amide}$), 1633 (NH), 1633 (C=C). ^{1}H NMR (DMSO-d_6): δ 7.97 (d, 1H, $J_{1,2}$=7.8 Hz, $H_{arom.}$-1) 7.85 (d, 1H, $J_{5,6}$=7.6 Hz, $H_{arom.}$-5), 7.62 (s, 1H, $H_{arom.}$-4), 7.59 (d, 1H, $J_{1,2}$=7.8 Hz, $H_{arom.}$-2), 7.30 (br s., 2H, $H_{arom.}$-5+$H_{arom.}$-8), 5.32 (t, 1H, $J_{6,7}$=2.2 Hz, $H_{androsta.}$-6), 4.07 (br s., 2H, 3-OH+*CH*-Me), 3.88 (s, 1H, 17-OH), 3.54 (s, 3H, OMe), 3.40 (m, 1H, H-17), 3.25 (m, 1H, H-3), 2.91 (m, 2H, $\underline{CH_2}$-CH_2-S), 2.75 (m, 2H, CH_2-$\underline{CH_2}$-S), 2.52 (m, 1H, H-15), 2.35 (m, 2H, H-4a+H-7a), 2.19 (m, 3H, H-4b+H-7b+H-16b), 1.71 (m, 4H, H-10a+CH-$\underline{Me}$), 1.61 (m, 3H, H-2a+H-11a+H-12a), 1.48 (m, 4H, H-1a+H-11b+H-12b+H-13), 1.24 (m, 3H, H-2b+H-8+H-9), 1.05 (m, 4H, H-1b+Me-19), 0.95 (s, 3H, Me-18). ^{13}C NMR (DMSO-d_6): δ 164.4 ($C_{oxadiazole}$-2), 160.4 ($C_{oxadiazole}$-5), 149.8 ($C_{arom.}$-OMe), 141.9 ($C_{androsten.}$-5), 138.3 ($C_{arom.}$-3), 135.3 ($C_{arom.}$-8a), 131.1 ($C_{arom.}$-4a), 130.4

($C_{arom.}$-5), 128.7 ($C_{arom.}$-2), 127.0 ($C_{arom.}$-4), 124.6 ($C_{arom.}$-1), 118.7 ($C_{arom.}$-6), 106.2 ($C_{arom.}$-8), 75.4 ($C_{androsten.}$-17), 67.4 ($C_{androsten.}$-3), 60.0 (OMe), 55.7 ($C_{androsten.}$-9), 48.9 ($C_{androsten.}$-14), 45.1 ($C_{androsten.}$-13), 44.7 ($C_{androsten.}$-4 + *CH*-Me), 37.1 ($C_{androsten.}$-1 + $C_{androsten.}$-10), 36.1 ($C_{androsten.}$-12), 34.2 ($C_{androsten.}$-16), 31.7 (CH_2CH_2S), 31.3 ($C_{androsten.}$-2 + $C_{androsten.}$-6 + $C_{androsten.}$-7), 30.7 ($C_{androsten.}$-8 + $C_{androsten.}$-15), 29.5 (CH_2CH_2S), 20.4 ($C_{androsta.}$-11 + CH*Me*), 18.7 (Me-19), 14.4 (Me-18). Anal. calc. for $C_{36}H_{46}N_2O4_2S$ (602.32): C, 71.73; H, 7.69; N, 4.65. Found: C, 71.73; H, 7.81; N, 4.71.

In vitro cytotoxic assay

The in vitro cytotoxic activity of MON and ABT against two human prostate cancer (PCa) cell lines, PC-3 (androgen receptor–negative) and LNCaP-AI (androgen receptor–positive), as well as the normal prostate epithelial cell line RWPE-1, was evaluated using the standard MTT assay (Mosmann 1983), as previously described. Briefly, the human PCa cell lines PC-3 and LNCaP-AI were obtained from the American Type Culture Collection (Rockville, MD). LNCaP-AI, PC-3, and RWPE-1 cells were cultured in RPMI medium supplemented with 5% fetal bovine serum (FBS, Gibco) and 1% penicillin–streptomycin. Cells were seeded into 96-well plates at a density of approximately 1.0×10^4 cells per well and incubated for 24 h under controlled conditions (37 °C, 5% CO_2). After incubation, the cells were treated with MON or ABT at a concentration of 10.0 µM (5 µL per well) for 48 h. The experimental setup included untreated control cells and blank wells without cells. Following a total incubation period of 72 h, 100 µL of MTT solution (2 mg/mL in PBS) was added to each well, and the plates were incubated for an additional 3 h at 37 °C in a humidified atmosphere containing 5% CO_2. The medium was then removed, and 100 µL of DMSO was added to dissolve the resulting purple formazan crystals for 10 min. Absorbance was measured at 570 nm using a spectrophotometer (Molecular Devices SpectraMax 190, USA). Each experiment was performed three times in quadruplicate.

Computational evaluations

DFT calculations

Density Functional Theory (DFT) calculations were performed to investigate the electronic structure and chemical reactivity of MON in comparison with ABT. All quantum chemical calculations were carried out using Gaussian 16W software (Frisch et al. 2016). The molecular geometries of both compounds were fully optimized using the B3LYP hybrid functional in conjunction with the 6–31 + G(d,p) basis set (Becke 1993). To verify that the optimized structures correspond to true minima on the potential energy surface, harmonic vibrational frequency calculations were conducted at the same level of theory, and the absence of imaginary frequencies was confirmed (Messaadia et al. 2020). Electronic properties relevant to molecular reactivity and intermolecular interactions were subsequently evaluated. Frontier Molecular Orbital (FMO) analysis was performed to determine the energies of the highest occupied molecular orbital (E_{HOMO}), the lowest unoccupied molecular orbital (E_{LUMO}), and the corresponding HOMO–LUMO energy gap (ΔE), which provides insight into chemical stability, electronic transitions, and potential biological activity. Molecular electrostatic potential (MEP) surfaces were generated to identify electron-rich and electron-deficient regions that may participate in non-covalent interactions with biological targets. Based on the FMO energies, global reactivity descriptors were calculated within the framework of conceptual DFT, including ionization potential (IP_E), electron affinity (EA), chemical potential (μ), global hardness (η), global softness (S), electronegativity (χ), and electrophilicity index (ω). The ionization potential and electron affinity were approximated as $-E_{HOMO}$ and $-E_{LUMO}$, respectively. The remaining descriptors were computed using the following equations (Bendaas et al. 2024):

$$\chi = -\mu = (IP_E + EA)/2 \quad (1)$$

$$\eta = (IP_E - EA)/2 \quad (2)$$

$$S = 1/(2\eta) \quad (3)$$

$$\omega = \chi^2/(2\eta) \quad (4)$$

To account for environmental effects, DFT calculations were performed in both the gas phase and in aqueous medium using the Conductor-like Polarizable Continuum Model (CPCM) (Takano and Houk 2005), thereby approximating physiological conditions. Visualization of optimized geometries, MEP maps, FMO distributions, and electronic density features was performed using GaussView 06 (Dennington et al. 2016).

Molecular docking

Molecular docking was performed to investigate the binding behavior and interaction profiles of MON in comparison with ABT, a clinically approved prostate cancer drug, against key protein targets implicated in prostate cancer progression and androgen signaling pathways (Castellan et al. 2019). The selected targets included epidermal growth factor receptor (EGFR, PDB ID: 1M17), cytochrome P450 17A1 (CYP17A1, PDB ID: 3RUK), and extracellular signal-regulated kinase 2 (ERK2, PDB ID: 4ZZN). The three-dimensional crystal

structures of these proteins were retrieved from the Protein Data Bank (PDB) (Berman 2000).

Prior to docking, protein structures were prepared by removing co-crystallized ligands, water molecules, and other heteroatoms, followed by the addition of polar hydrogen atoms. Kollman charges were assigned to the protein structures, while Gasteiger charges were applied to the ligands using AutoDock Tools (ADT) version 1.5.7 (Morris et al. 2009). All prepared structures were saved in PDBQT format.

The three-dimensional structures of MON and ABT were obtained from their geometry-optimized conformations derived from DFT calculations. Docking simulations were carried out using the Lamarckian Genetic Algorithm (LGA) implemented in AutoDock 4.2 (Morris et al. 2009). For all protein targets, a grid box of 70 × 70 × 70 points with a spacing of 0.375 Å was employed to adequately cover the active binding regions. The grid box centers were set at (20.085, 0.296, 52.815) for EGFR, (27.878, − 1.781, 32.252) for CYP17A1, and (− 15.575, 14.176, 42.346) for ERK2. For each docking experiment, 100 independent runs were performed to ensure sufficient conformational sampling. Docked poses were ranked according to predicted binding free energy (kcal/mol), and the lowest-energy conformation was selected as the most favorable binding mode for subsequent analyses (Bekkar et al. 2024; Benamor et al. 2025a; Bendaas et al. 2025).

To validate the reliability of the docking protocol, redocking of the co-crystallized ligands into their respective protein binding sites was performed, and the reproduced poses were compared with the corresponding experimental conformations (Bendaas et al. 2024; Benamor et al. 2025b). Key amino acid residues involved in ligand recognition and stabilization within the active sites were identified using PyMOL and the Protein–Ligand Interaction Profiler (PLIP) (Salentin et al. 2015; Schrödinger and DeLano 2020), based on interaction patterns observed for both the docked ligands and the native co-crystallized ligands.

ADMET and drug-likeness prediction

The pharmacokinetic and toxicity profiles of ABT and MON were assessed using in silico ADMET predictions. SwissADME and pkCSM web servers were used to evaluate drug-likeness, oral bioavailability, and gastrointestinal absorption, while ProTox-II was used to predict toxicity endpoints including acute toxicity, hepatotoxicity, and immunotoxicity (Pires et al. 2015; Daina et al. 2017; Banerjee et al. 2018). These tools provided complementary predictions for absorption, distribution, metabolism, excretion, and toxicity properties, which were analyzed to assess the pharmacokinetic suitability of the compounds.

Molecular dynamics simulation

Molecular dynamics (MD) simulations were performed to evaluate the conformational stability, dynamic behavior, and intermolecular interaction patterns of the selected protein–ligand complexes. The lowest-energy docked poses obtained from AutoDock were used as the initial coordinates for all simulations. MD simulations were conducted using GROMACS 2024 on a GPU-accelerated computing platform (Van Der Spoel et al. 2005).

The CHARMM36 force field was applied to describe the protein structures, while ligand topology files and force-field parameters for MON and ABT were generated using the SwissParam web server to ensure compatibility with the CHARMM force field (Bugnon et al. 2023). Each protein–ligand complex was placed in a cubic simulation box with a minimum distance of 10 Å from the box edge and solvated using the TIP3P water model, followed by the addition of appropriate Na^+ and Cl^- counterions to neutralize the system and mimic physiological ionic strength (Ayrim et al. 2025; Bekkar et al. 2025a). Energy minimization was performed using the steepest descent algorithm until the maximum force on any atom was reduced below 10.0 $kJ/mol^{-1}nm^{-1}$, thereby removing steric clashes and unfavorable contacts (Samah et al. 2025; Boudebia et al. 2025). The minimized systems were subsequently equilibrated in two stages. First, NVT equilibration was conducted for 100 ps at 300 K using the velocity-rescale (V-rescale) thermostat with a coupling constant of 0.1 ps. This was followed by NPT equilibration for 100 ps at 1 bar using the Berendsen barostat with a pressure coupling time of 2.0 ps, allowing system density stabilization (Adaika et al. 2025; Lanez et al. 2025). Following equilibration, production MD simulations of 100 ns were performed for each system under the NPT ensemble with periodic boundary conditions. Long-range electrostatic interactions were treated using the Particle Mesh Ewald (PME) method with a real-space cutoff of 12 Å, while van der Waals interactions were truncated at 12 Å using a force-switch smoothing function applied between 10 and 12 Å. Temperature was maintained at 300 K using the velocity-rescale thermostat, and pressure was controlled at 1 bar using the Parrinello–Rahman barostat. Trajectory coordinates were saved every 10 ps for subsequent analyses (Bekkar et al. 2025b; Abdul-Ridha et al. 2025; Abdul-Rida et al. 2026). Post-simulation analyses were carried out to assess the dynamic stability and structural integrity of the complexes. The root mean square deviation (RMSD) of the protein backbone was calculated to monitor overall system stability. Root mean square fluctuation (RMSF) analysis was performed to evaluate residue-level flexibility. The radius of gyration (Rg) was computed to examine the compactness of the protein structures, and the solvent-accessible surface area (SASA) was calculated to assess changes in protein surface exposure upon ligand binding. In addition, protein–ligand

hydrogen bonds were monitored throughout the simulations to evaluate their persistence and contribution to complex stability. Although replicate simulations were not performed, these analyses confirmed system convergence and overall stability, providing confidence that the observed interaction trends reflect equilibrated protein–ligand complexes.

MM/PBSA binding free energy and per-residue decomposition analysis

To complement the MD simulations and quantitatively evaluate ligand binding affinities, Molecular Mechanics Poisson–Boltzmann Surface Area (MM/PBSA) calculations were performed using the gmx_MMPBSA package (Kumari et al. 2014). Trajectory snapshots were extracted from the final 10 ns of each equilibrated MD trajectory at 10 ps intervals, yielding 1000 frames per system and providing adequate conformational sampling for statistically reliable free energy estimation.

The binding free energy (ΔG_{bind}) was calculated according to:

$$\Delta G_{Bind} = G_{complex} - (G_{protein} + G_{ligand}) \quad (5)$$

where $G_{complex}$, $G_{protein}$, and G_{ligand} represent the free energies of the protein–ligand complex, receptor, and ligand, respectively.

Each free energy term was further decomposed into molecular mechanics and solvation contributions as follows:

$$\Delta G = \Delta E_{Gas} + \Delta G_{solv} - T\Delta S \quad (6)$$

The gas-phase interaction energy (ΔE_{Gas}) consists of van der Waals (ΔE_{vdW}) and electrostatic (ΔE_{ele}) components, while the solvation free energy (ΔG_{solv}) includes a polar solvation term (ΔG_{PB}), computed using the Poisson–Boltzmann model, and a nonpolar solvation term (ΔG_{NPB}), estimated from the solvent-accessible surface area (SASA). The entropic contribution ($-T\Delta S$) was not included in the present analysis. This approximation is widely adopted in comparative MM/PBSA studies because entropy calculations are computationally expensive and often introduce substantial statistical noise, while having a limited impact on relative binding affinity trends between structurally related ligands (Gogoi et al. 2021). To identify key residues responsible for ligand stabilization and binding specificity, per-residue binding free energy decomposition was carried out within the MM/PBSA framework (Chaudhary and Aparoy 2020). This analysis partitions the total binding free energy into individual amino acid contributions, enabling residue-level interpretation of dominant hydrophobic, electrostatic, and polar interactions governing ligand recognition. Final MM/PBSA binding free energies and per-residue energy contributions were reported as mean ± standard deviation (SD) over all analyzed snapshots.

Conclusion

Monoxetanol (MON), a newly synthesized androstenediol derivative synthesized via a multistep route, demonstrated significant in vitro cytotoxic activity against human prostate cancer cell lines PC-3 and LNCaP-AI, with inhibition rates of 79.8% and 64.7% at 10.0 μM, respectively, while exhibiting negligible toxicity toward normal prostate epithelial cells. These findings establish a preliminary experimental basis for its anticancer potential. An integrated in silico strategy combining molecular docking, ADMET prediction, molecular dynamics (MD) simulations, MM/PBSA binding free energy calculations, and density functional theory (DFT) analyses was applied to assess the anticancer potential of MON relative to ABT. Molecular docking suggested that MON may exhibit stronger binding affinities than ABT toward key prostate cancer–related targets, including EGFR, CYP17A1, and ERK2, supported by favorable interactions with catalytically and regulatory important residues. While these docking results are predictive in nature and cannot alone confirm biological activity, they provide supportive evidence for the compound's potential. ADMET predictions indicated that MON possesses acceptable drug-likeness and no major toxicity alerts; however, its elevated molecular weight and lipophilicity may limit oral bioavailability, highlighting the need for formulation or structural optimization. MD simulations confirmed the dynamic stability of MON–protein complexes, as reflected by favorable RMSD, RMSF, radius of gyration, SASA, and hydrogen bond profiles. These observations were further supported by MM/PBSA calculations, which indicated favorable binding free energies primarily driven by van der Waals and electrostatic interactions. Per-residue energy decomposition highlighted broader and stronger stabilizing contributions for MON, particularly within the catalytic regions of CYP17A1 and ERK2. Complementary DFT analyses showed that MON possesses a larger HOMO–LUMO energy gap (ΔE) than ABT in both gas and aqueous environments, suggesting enhanced chemical stability and reduced intrinsic reactivity. Collectively, the convergence of experimental cytotoxicity, strong binding affinities, stable dynamic behavior, favorable energetic contributions, and robust electronic properties identifies MON as a promising lead compound for prostate cancer therapy. Further structural optimization, pharmacokinetic refinement, and in vivo validation are warranted to advance its development toward a viable therapeutic candidate.

Supplementary Information The online version contains supplementary material available at https://doi.org/10.1007/s40203-026-00626-3.

Acknowledgements We thank Prof. M.-F. Lin of Department of Biochemistry and Molecular Biology, University of Nebraska Medical Center, 985870 Nebraska, Medical Center, Omaha, NE 68198-5870, USA for assistance with the anticancer screening.

Author contributions Y.B. and L.Elh. measured and wrote the computational section, N.A.R. prepared Figs. 1–10, W.A.Al-M. and A.M.M. synthesized the compuonds 4–6 and steriod monoxetanol (MON, N.A.Al-M. supervised the project and wrote the mani manuscript text.

Data availability No datasets were generated or analysed during the current study.

Declarations

Conflict of interest The authors declare no conflict of interest.

References

Abdul-Rida NA, Farhan AM, Al-Masoudi NA, Saeed BA, Miller D, Lin M-F (2021) A novel pregnene analogs: synthesis, cytotoxicity on prostate cancer of PC-3 and LNCPa-AI cells and in silico molecular docking study. Mol Divers 25:661–671. https://doi.org/10.1007/s11030-020-10038-w

Abdul-Rida NA, Youssef NH, Allami RH, Bekker Y, Elhafnaoui L, Al-Masoudi NA (2026) Novel piperazine–pyrimidine hybrids as potential anticancer agents against MCF-7 breast carcinoma: synthesis, antimicrobial activity, antioxidant evaluation, and computational insights. J Mol Struct 1358:145287. https://doi.org/10.1016/j.molstruc.2026.145287

Abdul-Ridha NA, Youssef AM, Elhafnaoui L, Bekker Y, Al-Masoudi NA, Saeed BA, Al-Masoudi WA (2025) Synthesis, in-silico evaluation, ADME analysis, and molecular dynamics simulation of novel β-lactam derivatives based on diclofenac and sulindac with anticancer and antioxidant activities. Chem Biodivers 22:e01586. https://doi.org/10.1002/cbdv.202501586

Adaika A, Bekkar Y, Youmbai S, Bourougaa L, Lanez E, Benamor ML, Nesba K, Lanez T, Bechki L (2025) Synthesis, antioxidant, and antidiabetic potential of ferrocenylmethylnucleobase compounds: in vitro, in silico molecular docking, DFT calculation, and molecular dynamic simulations. Appl Organomet Chem 39:e7988. https://doi.org/10.1002/aoc.7988

Al-Masoudi NA, Abdul-Rida NA, Kadhim RA, Krug SJ, Engel M, Saeed BA (2016) Synthesis and CYP17α hydroxylase inhibition activity of new 3α- and 3β-ester derivatives of pregnenolone and related ether analogues. Med Chem Res 25:310–321. https://doi.org/10.1007/s00044-015-1480-z

Al-Masoudi NA, Ali DS, Saeed B, Hartmann RW, Engel M, Rashid S, Saeed A (2014) New CYP17 hydroxylase inhibitors: Synthesis, biological evaluation, QSAR, and molecular docking study of new pregnenolone analogs. Arch Pharm Chem Life Sci 347:1-12 https://doi.org/10.1002/ardp.201400255

Al-Masoudi NA, Kadhim RA, Abdul-Rida NA, Saeed BA, Engel M (2015a) New biaryl-chalcone derivatives of pregnenolone via Suzuki-Miyaura cross-coupling reaction. Synthesis, CYP17 hydroxylase inhibition activity, QSAR, and molecular docking study. Steroids 101:43–50. https://doi.org/10.1016/j.steroids.2015.05.011

Al-Masoudi NA, Mahdi KM, Abdul-Rida NA, Saeed BA, Engel M (2015b) A new pregnenolone analogues as privileged scaffolds in inhibition of CYP17 hydroxylase enzyme. Synthesis and in silico molecular docking study. Steroids 100:52–59. https://doi.org/10.1016/j.steroids.2015.05.002

Al-Masoudi NA, Sami A, Abdul-Rida NA, Fortscher M (2018) New cholic acid analogs: synthesis and 17β-hydroxydehydrogenase (17β-HSD) inhibition activity. Z Naturforsch B 73:211–223. https://doi.org/10.1515/znb-2018-0192

Ayrim NB, Balakit AA, Laftaa SJ, Alkazazz FF, Bekkar Y, Bourougaa L, Saleh BA (2025) Design, synthesis, and molecular docking studies of 2-azetidinone-based combretastatin A-4 analogues with anticancer activity. ChemistrySelect 10:e202405188. https://doi.org/10.1002/slct.202405188

Banday AH, Saeed BA, Al-Masoudi NA (2021) Synthesis, aromatase inhibitory, antiproliferative and molecular modeling studies of functionally diverse D-ring pregnenolone pyrazoles. Anti-Cancer Agents Med Chem 21(13):1671–1679. https://doi.org/10.2174/1871520620999201124213655

Banerjee P, Eckert AO, Schrey AK, Preissner R (2018) ProTox-II: a webserver for the prediction of toxicity of chemicals, Nucleic Acids Res 46:W257-W263. nar/gky318 https://doi.org/10.1093/

Becke AD (1993) Density-functional thermochemistry. III. The role of exact exchange. J Chem Phys 98:5648–5652. https://doi.org/10.1063/1.464913

Bekkar Y, Lanez E, Lanez T, Bourougaa L, Adaika A, Benine A, Saada Z (2025a) Combined in vitro and in silico analysis of ferrocenylmethylaniline derivatives: antibacterial potential, DFT calculations, and molecular dynamics insights. J Organomet Chem 1032:123618. https://doi.org/10.1016/j.jorganchem.2025.123618

Bekkar Y, Lanez E, Lanez T, Bourougaa L, Adaika A, Saada Z, Benine A (2025b) Antidiabetic potential of synthesized ferrocenylmethylaniline derivatives: insights from in vitro studies, molecular docking, ADMET, DFT calculations, and molecular dynamics simulation. Biotechnol Appl Biochem. https://doi.org/10.1002/bab.70014

Bekkar Y, Saada Z, Benine A (2024) Computational analysis of N-ferrocenylmethyl-N-phenylbenzohydrazide: molecular docking and dynamic stability with BSA. J Alger Chem Soc 1:29–43

Benamor ML, Lanez E, Bekkar Y, Adaika A, Lanez T, Nesba K, Bechki L (2025a) Evaluation of ferrocenylmethylnucleobases derivatives interacting with DNA: insights from electrochemical, spectroscopic, DFT calculation, molecular docking and molecular dynamic simulations. Stud Univ Babes-Bolyai Chem 70:111–132. https://doi.org/10.24193/subbchem.2025.1.08

Benamor ML, Lanez E, Bekkar Y, Adaika A, Lanez T, Nesba K, Bechki L (2025b) Exploring the interactions of ferrocenylmethylnucleobase derivatives with BSA and HHb: insights from electrochemical, spectroscopic, ADMET, in silico docking, and MD simulations. ChemistrySelect 10:1–16. https://doi.org/10.1002/slct.202404678

Bendaas R, Bekkar Y, Messaadia L, Bourougaa L, Messaoudi A, Kiamouche S, Messaoud B (2024) Computational-based investigation of antioxidative potential polyphenolic compounds of *Salvia officinalis* L.: combined DFT and molecular docking approaches. J Mol Model 30:87. https://doi.org/10.1007/s00894-024-05866

Bendaas R, Messaadia L, Bekkar Y, Bourougaa L, Messaoudi A (2025) Comprehensive in vitro and molecular docking analysis of antioxidant and antimicrobial properties of *Salvia officinalis* L. extracts and essential oils. J Mol Struct 1331:41621. https://doi.org/10.1016/jmolstruc.2025.141621

Berman HM (2000) The Protein Data Bank. Nucleic Acids Res 28:235–242. https://doi.org/10.1093/nar/28.1.235

Boudebia O, Benamor ML, Bourougaa L, Bekkar Y, Lanez E, Adaika A, Bouraoui R, Nesba K, Chaoua H, Hachani SE, Bechki L, Lanez T (2025) Holistic investigation of *Cotula cinerea* essential oil against diabetes: hypoglycemic activity, enzymatic inhibition, GC-MS characterization, ADMET forecasting, MD simulations, and DFT insights. J Comput Aided Mol des 39:80. https://doi.org/10.1007/s10822-025-00664-7

Bryce A, Ryan CJ (2012) Development and clinical utility of abiraterone acetate as an androgen synthesis inhibitor. Clin Pharmacol Ther 91:101–108. https://doi.org/10.1038/clpt.2011.275

Bugnon M, Goullieux M, Röhrig UF, Perez MAS, Daina A, Michielin O, Zoete V (2023) SwissParam 2023: a modern web-based tool for efficient small molecule parametrization. J Chem Inf Model 63:6469–6475. https://doi.org/10.1021/acs.jcim.3c01053

Castellan P, Castellucc M, De Nunzio C, Tema G, Primiceri G, Schips CL (2019) A drug safety evaluation of abiraterone acetate in the treatment of prostate cancer. Expert Opin Drug Saf 18:759–767. https://doi.org/10.1080/14740338.2019.1648428

Chaudhary N, Aparoy P (2020) Application of per-residue energy decomposition to identify the set of amino acids critical for in silico prediction of COX-2 inhibitory activity. Heliyon 6:e04944. https://doi.org/10.1016/j.heliyon.2020.e04944

Chen Y, Xin X, Li J, Xu J, Yu X, Li T, Mo Z, Hu Y (2013) RTK/ERK pathway under natural selection associated with prostate cancer. PLoS ONE 8:e78254. https://doi.org/10.1371/journal.pone.0078254

Chen Y, Zhang Q, Wang Q, Li J, Sipeky C, Xia J, Gao P et al (2017) Genetic association analysis of the RTK/ERK pathway with aggressive prostate cancer highlights the potential role of *CCND2* in disease progression. Sci Rep 7(1):4538. https://doi.org/10.1038/s41598-017-04731-4

Daina A, Michielin O, Zoete V (2017) SwissADME: a free web tool to evaluate pharmacokinetics, drug-likeness and medicinal chemistry friendliness of small molecules. Sci Rep 7:42717. https://doi.org/10.1038/srep42717

Dennington R, Keith TA, Millam JM (2016) GaussView, Version 6. Frisch MJ, Trucks GW, Schlegel HB, Scuseri G, Robb MA, Cheeseman JR, Scalmani G, et al. (2016) Gaussian 16, Revision B.01. Gaussian, Inc., Wallingford CT.

Frisch MJ, Truck GW, Schlegel HB, et al. (2016) Gaussian 16, Revision B.01. Gaussian, Inc., Wallingford.

Frisch MJ, Trucks GW, Schlegel HB, Scuseri G, Robb MA, Cheeseman JR, Scalmani G, et al. (2016) Gaussian 16, Revision B.01. Gaussian, Inc., Wallingford CT.

Gogoi B, Chowdhury P, Goswami N, Gogoi N, Naiya T, Chetia P, Mahanta S, Chetia D, Tanti B, Borah P, Handique PJ (2021) Identification of potential plant-based inhibitor against viral proteases of SARS-CoV-2 through molecular docking, MM-PBSA binding energy calculations and molecular dynamics simulation. Mol Divers 25:1963–1977. https://doi.org/10.1007/s11030-021-10211-9

Handratta VD, Vasaitis TS, Njar VC, Gediya LK, Kataria R, Chopra P, Newman D Jr, Farquhar R, Guo Z, Qiu Y, Brodie AM (2005) Novel C-17-heteroaryl steroidal CYP17 inhibitors/antiandrogens: synthesis, in vitro biological activity, pharmacokinetics, and antitumor activity in the LAPC4 human prostate cancer xenograft model. J Med Chem 48:2972–2984. https://doi.org/10.1021/jm040202w

Hartmann RW, Ehmer PB, Haidar S, Hector M, Jose J, Klein CDP, Seidel SB et al (2002) Inhibition of CYP 17, a new strategy for the treatment of prostate cancer. Arch Pharm Weinheim 335:119–128

Hu Q, Negri M, Olgen S, Hartmann RW (2010) The role of fluorine substitution in biphenyl methylene imidazole-type CYP17 inhibitors for the treatment of prostate carcinoma. ChemMedChem 5:899–910. https://doi.org/10.1002/cmdc.201000065

Kania E, Janica M, Nesterowicz M, Modzelewski W, Cybulski M, Janica J (2025) Advances and challenges in prostate cancer diagnosis: a comprehensive review. Cancers 17:2137. https://doi.org/10.3390/cancers17132137

Kmeťová Sivoňová M, Jurečeková J, Tatarková Z, Kaplán P, Lichardusová L, Hatok J (2017) The role of CYP17A1 in prostate cancer development: structure, function, mechanism of action, genetic variations and its inhibition. Gen Physiol Biophys 36:487–499. https://doi.org/10.4149/gpb_2017024

Kumari R, Kumar R, Lynn A (2014) g_mmpbsa —a GROMACS tool for high-throughput MM-PBSA calculations. J Chem Inf Model 54:1951–1962. https://doi.org/10.1021/ci500020m

Lanez E, Bekkar Y, Bourouga L, Bourougaa L, Benamor ML, Bouraoui R, Boudebia O et al (2025) Antidiabetic potential of mentha piperita essential oil: GC-MS profiling, in vitro, in vivo and in silico analyses. J Mol Struct 1351:44239. https://doi.org/10.1016/j.molstruc.2025.144239

Messaadia L, Bekkar Y, Benamira M, Lahmar H (2020) Predicting the antioxidant activity of some flavonoids of *Arbutus* plant: a theoretical approach. Chem Phys Impact 1:100007. https://doi.org/10.1016/j.chphi.2020.100007

Moreira VMA, Vasaitis TS, Guo Z et al (2008b) Synthesis of novel C17 steroidal carbamates. Steroids 73:1217–1227. https://doi.org/10.1016/j.steroids.2008.05.010

Moreira V, Salvador J, Vasaitis T, Njar V (2008a) CYP17 inhibitors for prostate cancer treatment–an update. Curr Med Chem 15:868–899. https://doi.org/10.2174/092986708783955428

Morris GM, Huey R, Lindstrom W et al (2009) AutoDock4 and AutoDockTools4: automated docking with selective receptor flexibility. J Comput Chem 30:2785–2791. https://doi.org/10.1002/jcc.21256

Mosmann T (1983) Rapid colorimetric assay for cellular growth and survival: application to proliferation and cytotoxicity assays. J Immunol Methods 65:55–63. https://doi.org/10.1016/0022-1759(83)90303-4

Njar VCO, Kato K, Nnane IP, Grigoryev DN, Long BJ, Brodie AMH (1998) Novel 17-azolyl steroids, potent inhibitors of human cytochrome 17α-hydroxylase-C17,20 -lyase (P450 17α:potential agents for the treatment of prostate cancer. J Med Chem 41:902–912. https://doi.org/10.1021/jm970568r

Pires DEV, Blundell TL, Ascher DB (2015) pkCSM: predicting small-molecule pharmacokinetic and toxicity properties using graph-based signatures. J Med Chem 58:4066–4072. https://doi.org/10.1021/acs.jmedchem.5b00104

Potter GA, Barrie SE, Jarman M, Rowlands MG (1995) Novel steroidal inhibitors of human cytochrome P45017 alpha (17 alpha-hydroxylase-C17,20-lyase): potential agents for the treatment of prostatic cancer. J Med Chem 38:2463-71. jm00013a022 https://doi.org/10.1021/

Salentin S, Schreiber S, Haupt VJ, Adasme MF, Schroeder M (2015) PLIP: fully automated protein–ligand interaction profiler. Nucleic Acids Res 43:W443–W447. https://doi.org/10.1093/nar/gkv315

Samah B, Lanez E, Benamor ML, Bekkar Y, Salah NN, Bourougaa L, Bouraoui R, Garzoli S, Lanez T (2025) GC/MS analysis and computational evaluation of *C. cinerea* EO constituents for colorectal cancer: molecular docking, dynamics, and quantum chemical insights into cis-verbenyl acetate. Comput Biol Chem 120(Pt 2):108754. https://doi.org/10.1016/j.compbiolchem.2025.108754

Schlomm T, Kirstein P, Iwers L, Daniel B, Steuber T, Walz J et al (2017) Clinical significance of epidermal growth factor receptor protein overexpression and gene copy number gains in prostate cancer. Clin Cancer Res 13:6579–6584. https://doi.org/10.1158/1078-0432.CCR-07-1257

Schrödinger LLC, DeLano W (2020) PyMOL (2.4.0). http://www.pymol.org/pymol.

Takano Y, Houk KN (2005) Benchmarking the conductor-like polarizable continuum model (CPCM) for aqueous solvation free energies of neutral and ionic organic molecules. J Chem Theory Comput 1:70–77. https://doi.org/10.1021/ct049977a

Van Der Spoel D, Lindahl E, Hess B, Groenhof G, Mark AE, Berendsen HJC (2005) GROMACS: fast, flexible, and free. J Comput Chem 26:1701–1718. https://doi.org/10.1002/jcc.20291

Vasaitis T, Belosay A, Schayowitz A, Khandelwal A, Chopra P, Gediya LK, Guo Z, Fang H-B, Njar VCO, Brodie AMH (2008) Androgen receptor inactivation contributes to antitumor efficacy

of 17α-hydroxylase/17,20-lyase inhibitor 3β-hydroxy-17-(1H-benzimidazole-1-yl)androsta-5,16-diene in prostate cancer. Mol Cancer Ther 7(8):2348–2357. https://doi.org/10.1158/1535-7163.MCT-08-0230

Vasaitis TS, Bruno RD, Njar VCO (2011) CYP17 inhibitors for prostate cancer therapy. J Steroid Biochem Mol Biol 125:23–31. https://doi.org/10.1016/j.jsbmb.2010.11.005